

Characterizing the Growth Rate of a Corrosion Layer on Stainless Steel in a Molten Salt Environment

A thesis submitted in partial fulfillment of the requirement
for the degree of Bachelor of Science in Physics from
The College of William and Mary

by

Calvin Ernest Hensler

Accepted for _____
(Honors or no-Honors)

William Cooke, Director

Gina Hoatson, Physics

Mainak Patel, Mathematics

Williamsburg, VA
May 2, 2017

Characterizing the Growth Rate of a Corrosion Layer on Stainless Steel in a Molten Salt Environment

Calvin Hensler
Advisor: William Cooke
May 2, 2017

Abstract

Solar central receiver power plants are an up-and-coming clean energy option which make use of concentrated solar power. In order to function, these systems must be able to store molten “solar salt” (40% potassium nitrate, 60% sodium nitrate), which has proven to be highly corrosive to stainless steel. Slowing the corrosion rate of stainless steel when exposed to molten salt would be a significant step in the feasibility and cost-effectiveness of solar central receiver power plants, but in order to test the effectiveness of various treatments, we first need a method of characterizing the thickness of the corrosion layer. We have developed a means of determining the thickness of the corrosion layer by examining the oxygen and iron content at varying depths of a stainless steel sample exposed to molten salt using energy dispersive x-ray spectroscopy at varying accelerating voltages, enabling a non-invasive, non-destructive technique for this necessary characterization.

Contents

1	Introduction	4
1.1	Solar Power Towers.....	4
1.2	The Molten Salt Threat.....	5
1.3	Electropolishing Stainless Steel.....	8
1.4	Characterizing the Growth Rate of the Corrosion Layer.....	12
2	Methods	12
2.1	Experimental Methods.....	12
2.1.1	Samples.....	12
2.1.2	Cleaning.....	15
2.1.3	Electropolishing.....	15
2.1.4	Molten Salt Exposure.....	16
2.1.5	Energy Dispersive X-Ray Spectroscopy.....	17
2.2	Analytical Methods.....	19
2.2.1	Shift Analysis.....	19
2.2.2	Conversion Constant.....	20
3	Results	21
3.1	The Oxygen to Iron Ratio.....	21
3.2	Depth Characterization.....	24
3.3	Comparing with Bradshaw and Goods.....	31
4	Discussion	35
5	Conclusion	37
	Acknowledgments	38
	References	39

1 Introduction

1.1 Solar Power Towers

Solar Power Towers, also called Central Tower or Heliostat Power Plants, use an array of mirrors to concentrate sunlight onto a central tower. Early models of this concept used the solar energy to heat up a reservoir of water directly, which would then boil and turn turbines to produce energy; however, an agent which is able to reach higher temperatures can produce more energy. For this reason, more recent actualizations of this concept have been using a molten mixture of 40% potassium nitrate and 60% sodium nitrate, colloquially called “solar salt,” in order to increase the efficiency of the power plants.

In the solar salt Heliostat Power Plant, the central tower connects to two reservoirs of molten salt: a hot tank at 565°C and a cold tank at 350°C. Molten solar salt from the cold reservoir flows through the central tower where the concentrated sunlight heats the salt to 565°C; the molten salt then flows back to the hot tank. Next, the salt moves from the hot tank to the steam generator, which transfers the heat from the solar salt to the water, producing steam that turns a turbine, producing electricity. Now cooled to 350°C, the molten salt flows from the steam generator to the cold reservoir to repeat the cycle. A schematic overviewing this process is shown in Figure 1 [7].

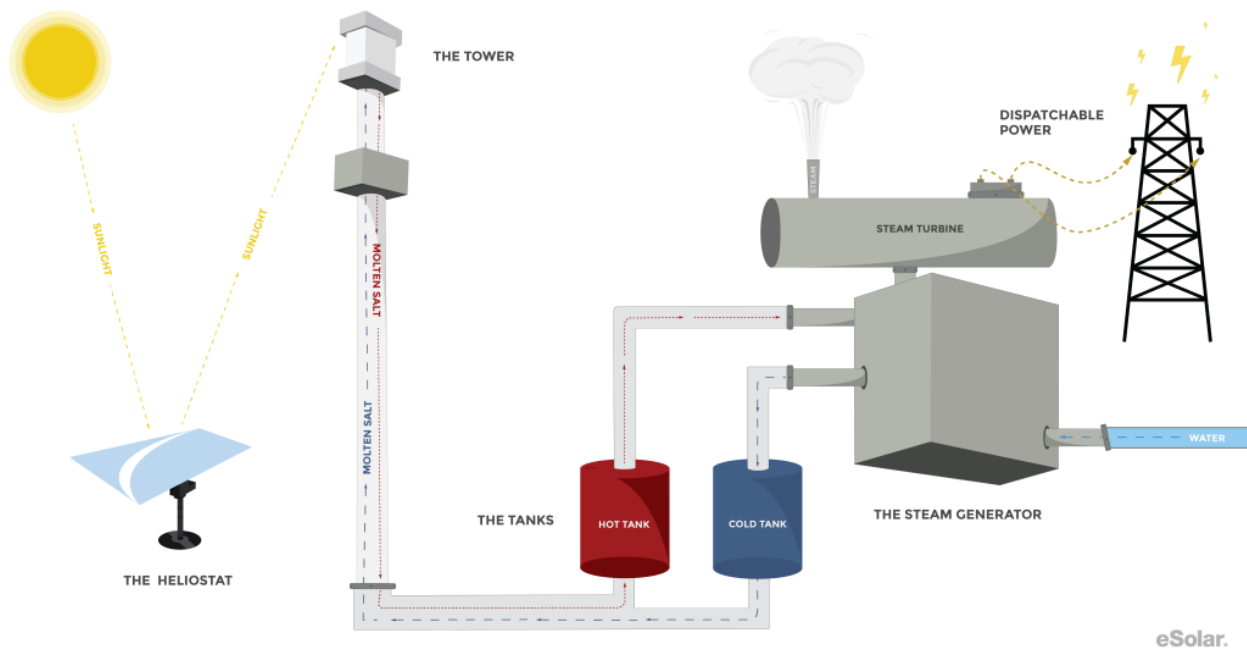


Figure 1: Heliostat Power Plant schematic

1.2 The Molten Salt Threat

While the physical properties of the molten nitrate mix have been useful in increasing efficiency, the molten salt is extremely corrosive, damaging the pipes and storage units the salt is contained in. A corrosion layer forms, eventually threatening junctions as well as the integrity of the system at large; thus, there is a need for an inexpensive material that is resistant to the corrosive nature of molten solar salt. Stainless steel is cheap and easy to produce but has been proven to corrode quickly when exposed to the molten nitrates; however, if the steel could be treated in such a way that improves its resistance to this effect, Solar Power Towers would become a much more cost-effective option for clean energy.

Figures 2 and 3 show Stainless Steel before and after exposure to molten salt, displaying the corrosion layer that forms over time.

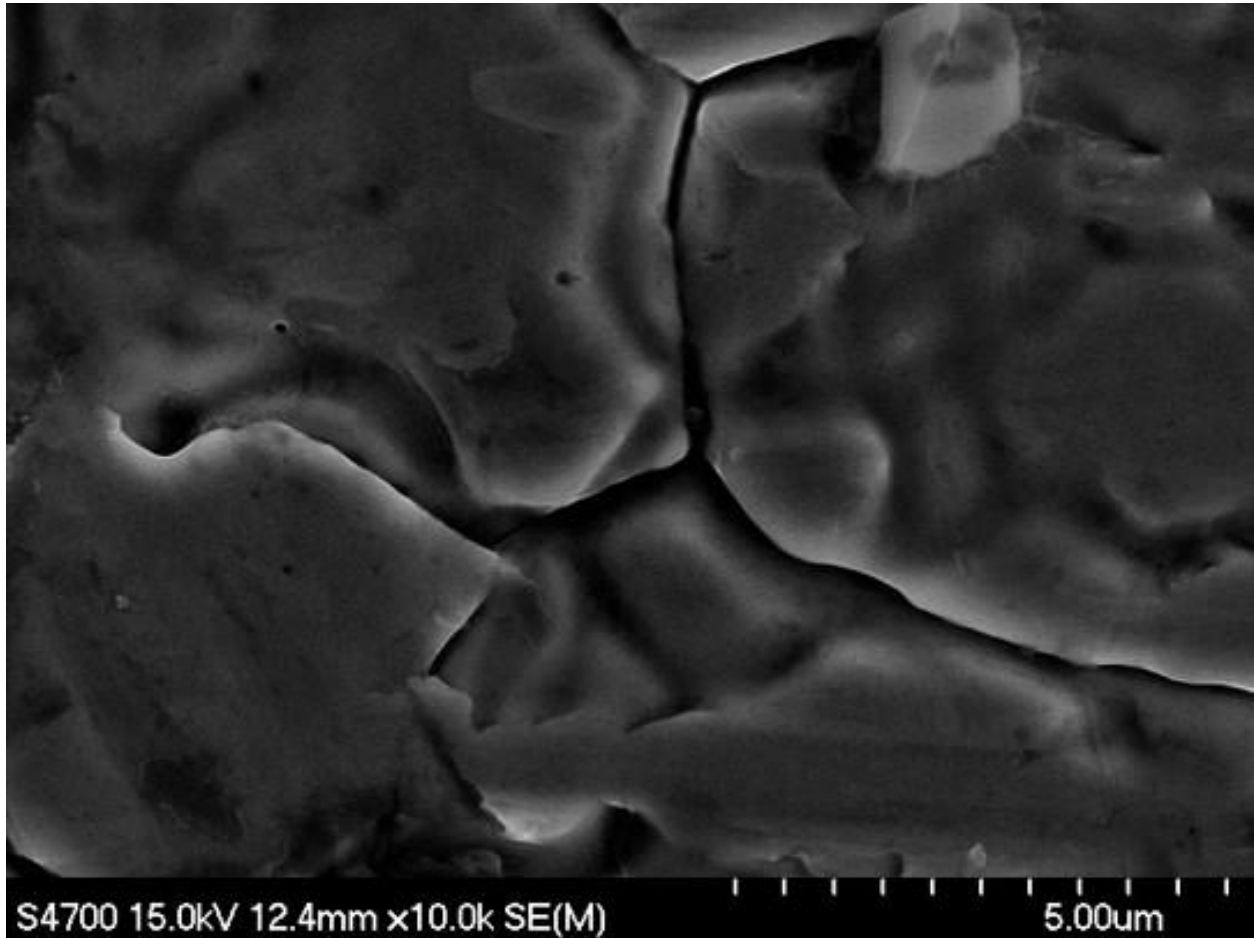


Figure 2: FE-SEM image of Stainless Steel 316 sample as-received

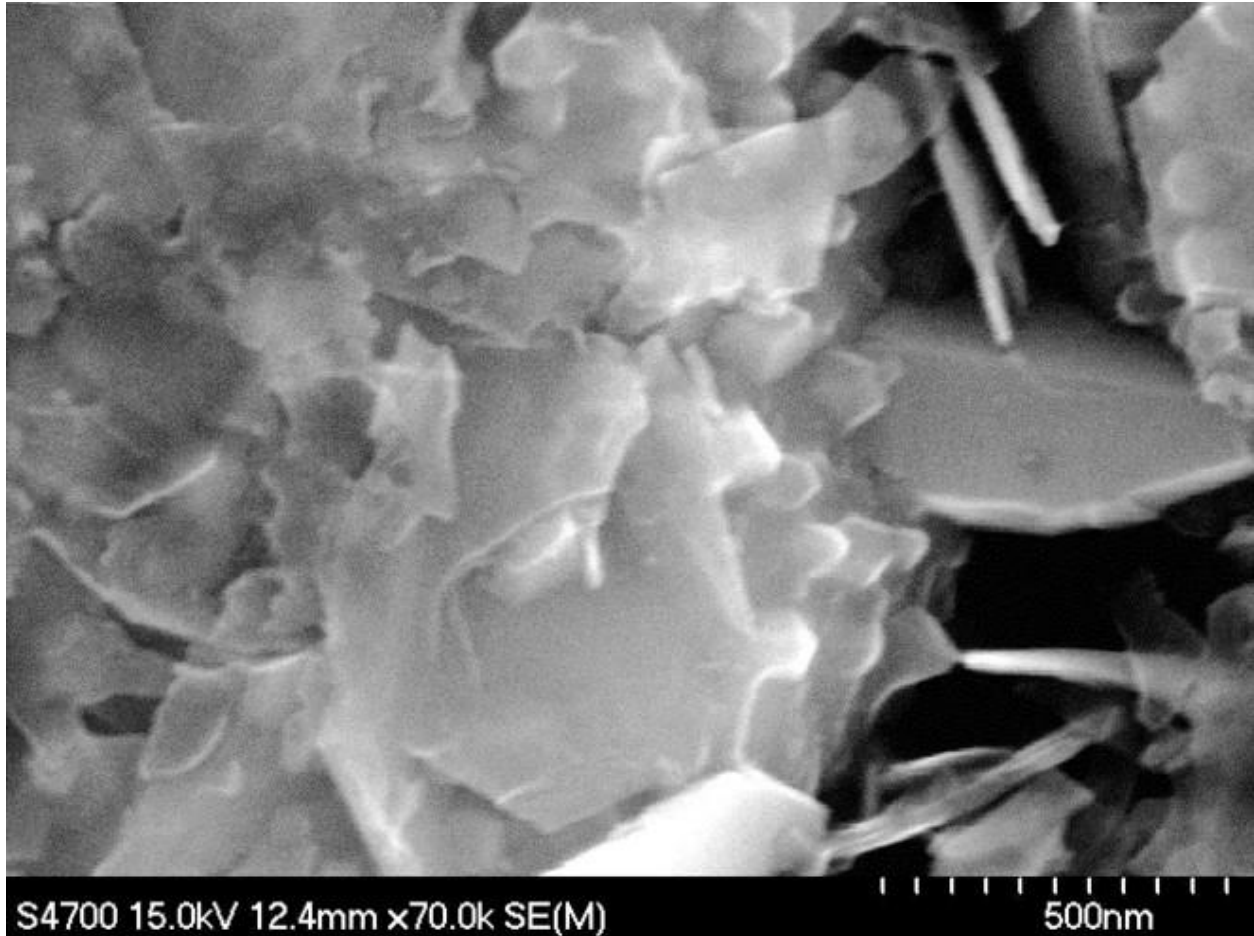


Figure 3: FE-SEM image of Stainless Steel 316 sample after 180 minute exposure to molten salt at 565°C

1.3 Electropolishing Stainless Steel

Electropolishing is an electrochemical process which treats a metal surface without applying any stress to it. The effect is the opposite of electroplating; electropolishing deburrs the surface of the metal, favoring the outermost protrusions and leaving a level surface as well as providing it with a chromium oxide coating. By using the sample one wishes to polish as an anode connected to the positive terminal of a direct current source in an electrolyte bath, the surface of the sample is oxidized. The cathode undergoes a reduction reaction and is plated as the sample is polished. The oxide coating left on the sample is claimed to improve resistance to corrosion. This increased resistivity to corrosion has been tested on Stainless Steel 316 exposed to a hot salt water spray: a sample that has not been electropolished endures 8 hours of exposure to the spray, whereas an electropolished sample lasts between 500 and 2700 hours before showing signs of corrosion [4].



Figure 4: Our Electropolishing Setup, including electropolish solution (left) and power source (right).

A grain boundary is the naturally-forming boundary between regions of a solid crystalline material. Where two structures of the same composition meet, there is a discontinuity with a width of about two atomic diameters which is called the homophase or grain boundary. An as-received sample, that is, a sample that comes from the manufacturer and has not been treated or polished in any way, has deep, prominent grain boundaries, where we expect corrosion layers form preferentially. These grain boundaries are primarily the result of the rolling process used to produce sheets of the steel. By treating a stainless steel sample with electropolishing, we can eliminate defects caused during production, leaving a smooth surface and exposing the natural grain boundaries of the metal. This is useful for examining the early stages of growth of polycrystalline films that form as a result of molten salt exposure. By creating a smooth surface, we expect the formation of the corrosion layer to be more consistent and quantifiable at early timescales (namely, the first 200 hours) than the formation on a sample still showing the crude surface produced in the factory; as such, we have treated all of the samples used in our analysis with electropolishing.

Figures 5 and 6 show unpolished and polished stainless steel 316. In the unpolished steel, there are deep crevices throughout the pictured region: these are the manufactured grain boundaries that we seek to eliminate. The polished sample pictured in Figure 6 shows the shallow, natural grain boundaries exposed by the electropolishing process.

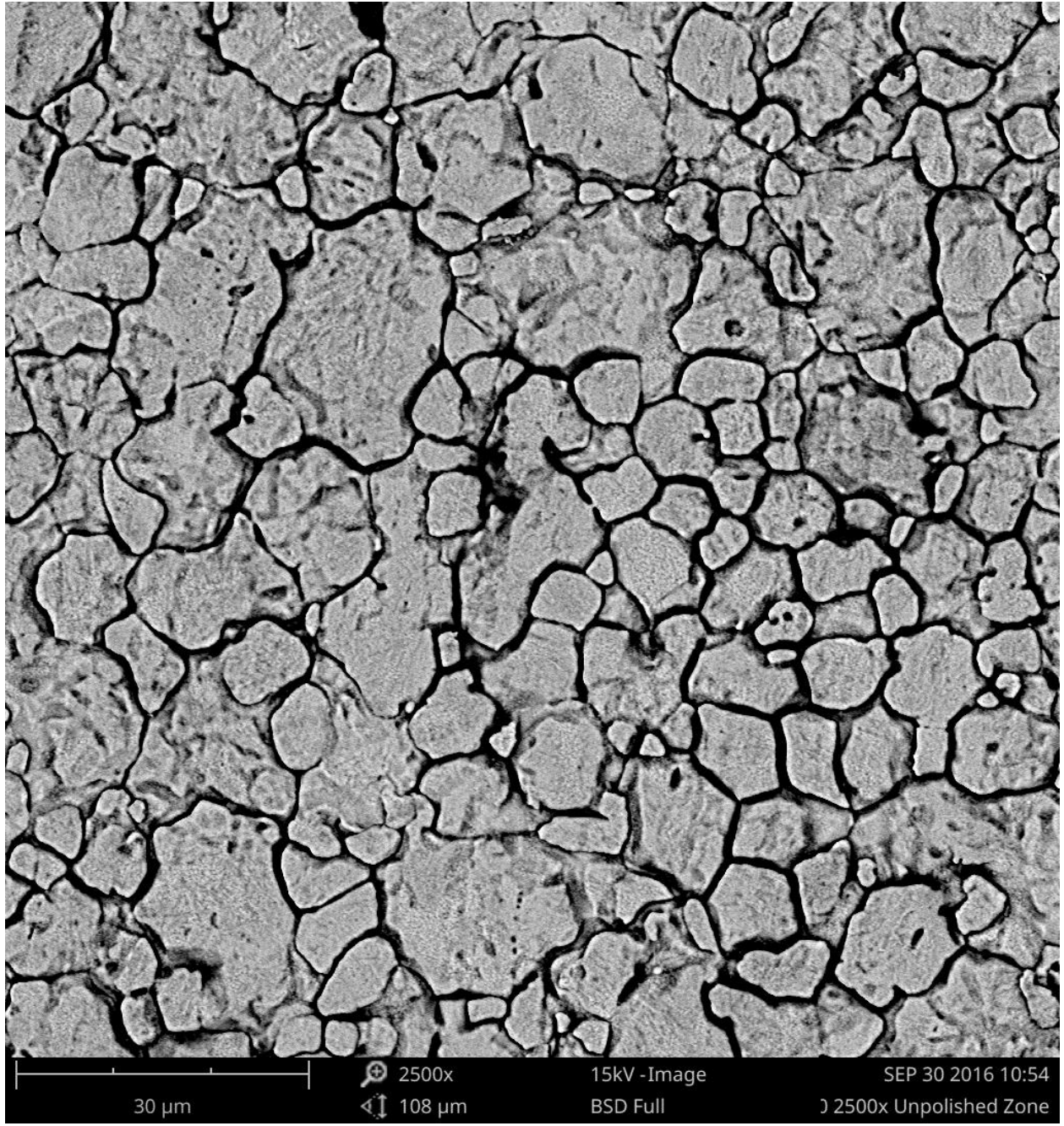


Figure 5: Unpolished Stainless Steel 316

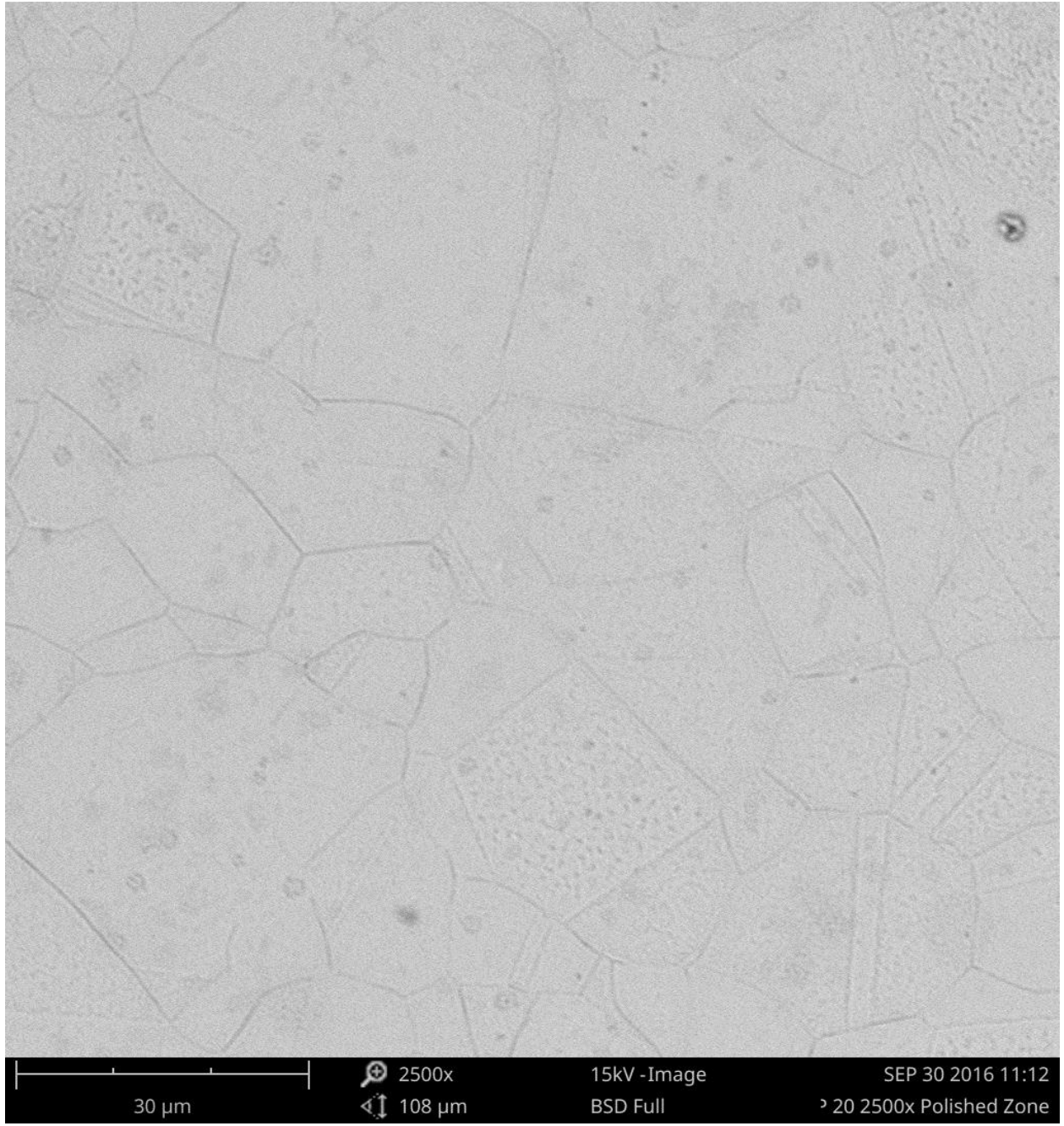


Figure 6: Electropolished Stainless Steel 316

1.4 Characterizing the Growth Rate of the Corrosion Layer

Before we are ready to look into surface treatment, we need to be able to characterize the growth of the oxide layer. Though Bradshaw and Goods have been able to achieve this by descaling the corrosion layer in a boiling alkaline permanganate, we seek to develop a non-destructive technique [5].

We hypothesize that, by using Energy-Dispersive X-Ray Spectroscopy (EDS) to look at the ratio of the oxygen content to the iron content at different accelerating voltages across various times within the first 200 hours of exposure to molten salt, we can characterize the growth rate of the corrosion layer on Stainless Steel 304 samples and verify these results by comparing them to the iron loss measurements reported by Goods and Bradshaw in their paper, "Corrosion Resistance of Stainless Steels During Thermal Cycling in Alkali Nitrate Molten Salts," all without causing any damage to the samples used.

2 Methods

2.1 Experimental Methods

2.1.1 Samples

The samples we use are 1 cm wide, 2 cm long, and .8mm thick, weigh about 1g, and are given distinctive markings to help us identify the type of stainless steel (we have worked with Stainless Steel 304, 316, and 347 throughout the course of the project). Marked samples are shown in Figure 7, and the properties of the various types of stainless steel are shown in Figure 8.



Figure 7: Samples distinctively marked. From left to right: Stainless Steel 304, Stainless Steel 316, and Stainless Steel 347

Element	Maximum % Composition
Carbon	.08
Manganese	2
Phosphorus	.0045
Sulfur	.03
Silicon	.75
Chromium	20
Nickel	12
Nitrogen	.1
Iron	Balance

Figure 8: Stainless Steel 304 Properties [1]

For the majority of the project, we used Stainless Steel 304 (SS304) for our analysis in order to compare to the work of Bradshaw and Goods, who also used SS304 for their analysis.

The formalism used to name a sample involves two letters and a number. If a sample is unpolished, its name begins “UP.” If a sample is electropolished, its name begins “EP.” The numbers are assigned beginning with 1 and ascending chronologically, so the fifteenth electropolished sample would be called “EP 15.” After exposure, a sample’s name and exposure time are inscribed using a laser marker as shown in Figure 9. A cross is also inscribed for analysis purposes which will be covered in more detail in Section 2.1.5.



Figure 9: EP 23 laser marked after 120 minute exposure

2.1.2 Cleaning

Each piece of equipment that comes into contact with the samples, including the samples themselves, undergoes the same cleaning routine. This cleaning process involves a 4-minute ultrasonic rinse in a sanitary container filled with deionized water, a 4-minute vibrating clean in a Sparkleen and deionized water solution, two 4-minute rinses in fresh deionized water, and drying with a heat gun. This process is designed to remove any contaminants without damaging the surface of the samples or equipment. This rigorous cleaning process is a precaution. Energy Dispersive X-Ray Spectroscopy measures a bulk, so surface contamination should not be much of a problem; however, we did our best to remove contaminants anyway.

2.1.3 Electropolishing

The process that we use to electropolish a sample before exposure to molten salt is as follows. First, we soak the sample in 28% Nitric Acid (HNO_3) for 15 minutes; this is a passivation process, which reduces iron levels and produces an oxide coating. We then rinse the sample with deionized water and move the sample directly to the electropolish. The sample is clamped to a stainless steel rod with 1 cm submerged in the electropolish bath. The rod extends through the lid of the apparatus shown in Figure 4 above. This rod is attached to the positive terminal of the power source, which is set to .5 Amp for a coupon of this size, yielding a current density of $.25 \text{ A/cm}^2$. Also submerged in the electropolish is a conducting rod connected to the negative terminal of the power source; this rod is plated while the sample is polished. The electropolish is kept at around $44 (\pm 1) \text{ }^\circ\text{C}$. After electropolishing, the sample is rinsed with deionized

water, rinsed with isopropanol, and cleaned using the process described in Section 2.1.2. It is important to note the safety concerns with regards to the electropolishing process. The nitric oxide produced when electropolishing takes place is potentially fatal if inhaled; furthermore, the electropolish solution itself will burn surfaces it comes into contact with, so proper ventilation as well as foot, eye, and hand protection are necessary for the duration of the treatment.

The results of electropolishing are shown in high magnification in Figure 6; however the effect is quantifiable. Figure 10 shows the roughness in microns of both a polished and an unpolished sample as a function of horizontal position along the sample in millimeters.

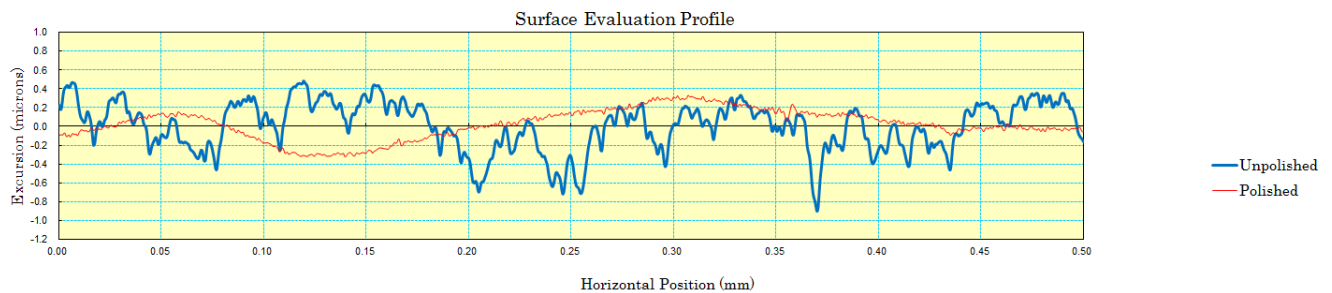


Figure 10: Graph of roughness of polished (red) and unpolished (blue) Stainless Steel 304

2.1.4 Molten Salt Exposure

Exposure to the molten salt involves high temperatures, so heat protection and extreme care are necessary during this process. First, the appropriate mixture (a mass ratio of 2:3) of potassium nitrate and sodium nitrate is used to fill alumina crucibles up to a depth of about 1 cm. Next, the crucibles and the salt are placed in the oven and baked at 200°C for 4 hours. This step removes any water that may have accumulated

on the materials. Next, the temperature of the oven is increased to 565°C, and the solar salt is melted over the course of 90 minutes. Lastly, the samples are placed in the now molten salt and the oven is closed. After the desired exposure time, the samples are removed from the salt and allowed to cool; they are then cleaned and analyzed. Our oven is pictured with five crucibles inside in Figure 11.

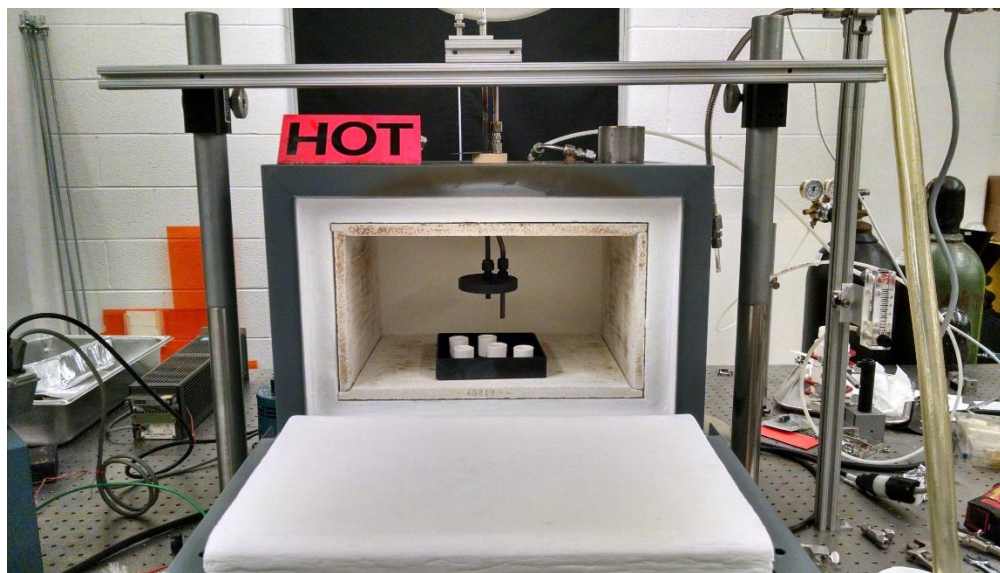


Figure 11: Oven with alumina crucibles filled with molten salt

2.1.5 Energy Dispersive X-Ray Spectroscopy

Our quantitative analysis was completed using Energy Dispersive X-ray Spectroscopy (EDS). EDS is a method of analysis which enables us to identify the elemental composition of samples; it is particularly useful because it produces normalized, quantitative measurements of the content of various elements on the surface of the sample, which allows us to examine how much oxygen and iron exist within a given depth of the sample's bulk: a critical element of our corrosion layer depth characterization model.

When conducting EDS, an electron beam is focused onto the sample being analyzed. This excites an electron in the inner shell, sending it off from the shell and allowing an electron from a higher-energy shell to take its place; this process emits an X-ray of a specific energy based on the element in which the excitation occurred. By counting the number of X-rays emitted at various energies, the elemental composition of the sample can be determined. We take 4 measurements at 15kV and 4 measurements at 25kV at either 5k or 10k magnification. We examined data sets at each magnification and saw no difference. 5k magnification shows an area of $400\mu\text{m}^2$, and 10k magnification shows an area of $100\mu\text{m}^2$.

EDS produces a spectrum which consists of a number of counts within a .01 keV bin, as shown in Figure 12. By examining the energies at which peaks develop, the counts can be interpreted as atomic percentages.

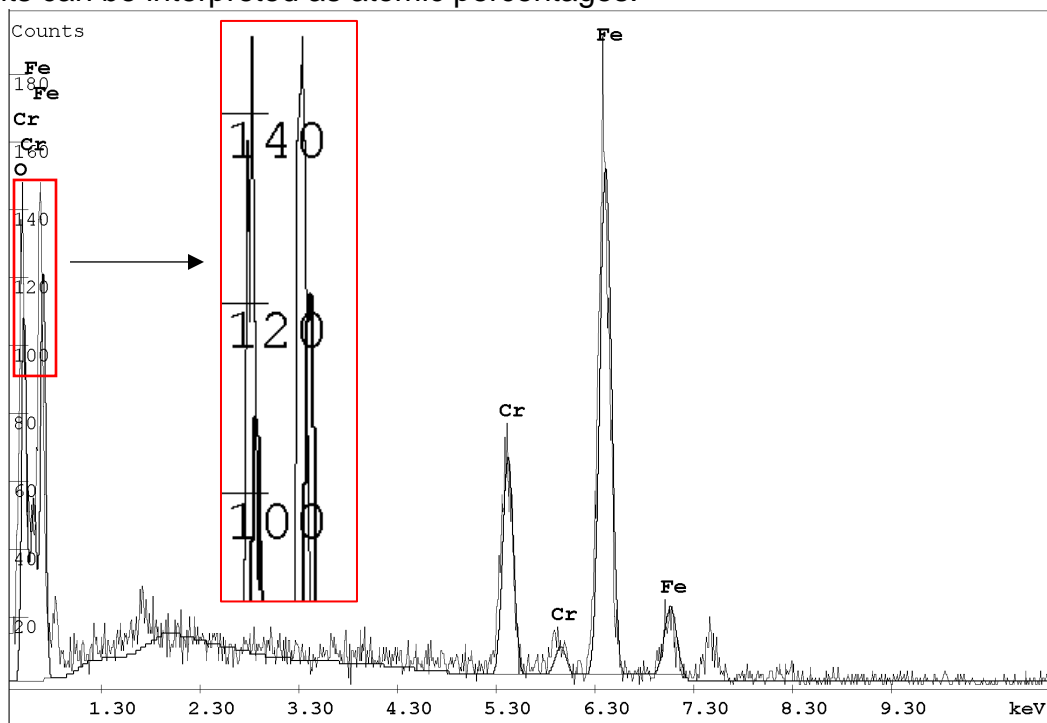


Figure 12: EDS Spectrum of EP 18

2.2 Analytical Methods

2.2.1 Shift Analysis

Scientists have reservations about using EDS as a quantitative analytical technique. In order to be sensitive to this skepticism throughout the completion of this project, we were thorough in our examination of the data produced by this technique, namely with regards to peak misalignment.

In the early stages of our analysis, we noticed some chronic misalignment between the actual spectrum produced and the fit that the EDS assigned to this spectrum, indicating some calibration error within the EDS that we were unable to address directly.

This misalignment has the potential to be problematic for our analysis, as the accuracy of the oxygen and iron content as measured by the EDS depends on how well the fit matches the spectrum created by the counts of x-rays at a given energy recorded. In order to tackle this potential issue, we took various spectra and shifted them by increments of .01 keV to the left and right, examining the iron and oxygen content in each new spectrum. This study allowed us to understand the sensitivity of our quantitative measurements to the misalignment of the peaks.

Ultimately, we determined that the misalignment was not an issue that we needed to be concerned about. While there is an obvious dependence of the number of counts on the energy offset, in the case of both oxygen and iron, the effect is orders of magnitude less than the standard deviation between measurements.

Figure 13 shows the sensitivity of the integrated counts to the shift in energy.

While it is clear from these graphs that a significant misalignment would result in a large drop in integrated oxygen counts, by shifting the spectra to within one bin of the actual peak, we would fall within the upper regime, where the counts do not vary much.

Furthermore, while estimating error at the final stages of the depth characterization, we discovered that the contribution of the misalignment was orders of magnitude less than that of the statistical variation.

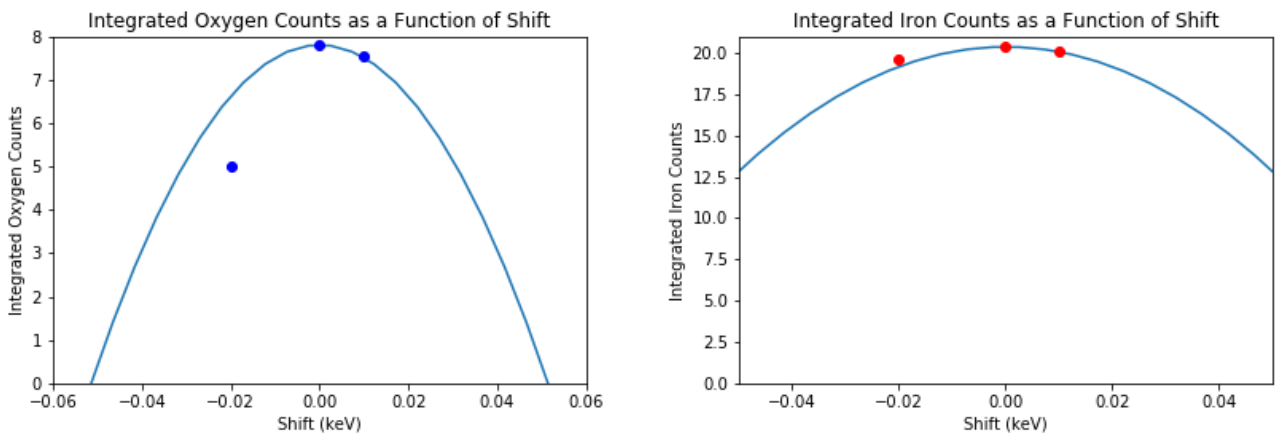


Figure 13: Graph of Integrated Oxygen and Iron Counts as a function of Energy Shift

2.2.2 Conversion Constant

To convert atomic percentages produced by the EDS into counts and vice versa, we conducted a thorough analysis of exactly how they were produced. The data collected in its most basic form is a counted number of x-rays at measurable energies; however, the EDS software uses Gaussian integration in order to get from counts to integrated counts. We had to determine the conversion constant in order to get the amount of iron or oxygen from the shifted spectra.

To unearth the method used by the EDS to convert from integrated counts to atomic percentages, we looked at the ratio of the given atomic percentages divided by the ratio of the given integrated counts. By doing this across numerous spectra, we discovered that the scaling factor between these ratios was a constant unique to the accelerating voltage at which the measurement was taken. For our analysis, we looked at spectra taken at 15kV and 25kV, which yielded conversion constants of $1.21 \pm .03$ and $5.26 \pm .14$. These factors are used to switch between atomic percentages and integrated counts, as well as to play a role in the error analysis.

3 Results

3.1 The Oxygen to Iron Ratio

We have chosen to characterize the depth of the oxide layer is using the ratio of the oxygen content to the iron content. We expect this ratio to be a useful based on two assumptions. First, we assume that as the corrosion layer forms, we will not lose any iron to the molten salt in the process. Second, we assume that as the corrosion layer forms, we will see an increase in oxygen. These assumptions are based both on what we know to be true about the formation of oxides as well as what we have observed in years previous as reported by Samuel Girdzis in his paper, "Corrosion in a Molten Salt Environment." Should these assumptions hold, it is reasonable to consider the ratio of oxygen, which appeared during the formation of the corrosion layer, to iron, which has remained constant throughout the process, as an indicator of the depth of the oxide layer formed. As such, we began our analysis by examining this ratio as a function of exposure time.

Because oxygen proceeds through the corrosion layer to the steel below in a random walk, the time dependence of the growth rate should be quadratic, meaning that the dependence of the ratio on the square root of time should be linear.

Figure 14 shows a basic electron penetration depth model in which region A is the corrosion layer and region B is the stainless steel. Electrons with more energy will penetrate deeper into the sample. If a beam does not penetrate all the way through the corrosion layer, we call this “saturation.”



Figure 14: Electron depth penetration model

Figures 15 and 16 show the oxygen to iron ratio of samples analyzed at 15kV and 25kV as well as a dotted line which marks the expected saturation point: the depth we expect the electron beam to penetrate into a bulk of corrosion. Looking at the oxygen to iron ratios shown in Figure 15 can be slightly misleading; the conversion constant used to extract counts from reported atomic percentages results in a stretch of the y-axis. The conversion constant for 25kV is smaller than that of 15kV by a factor of 4; knowing this, we can verify that the 200 hour sample is consistent between both accelerating voltages: the electrons still have not penetrated the corrosion layer formed over that time scale.

By examining the 20 hour exposure results, we see an oxygen to iron ratio of ~1.5, indicating that the oxide layer formed is likely Hematite, or Fe_2O_3 . This will be an important element of the depth characterization in Section 3.2.

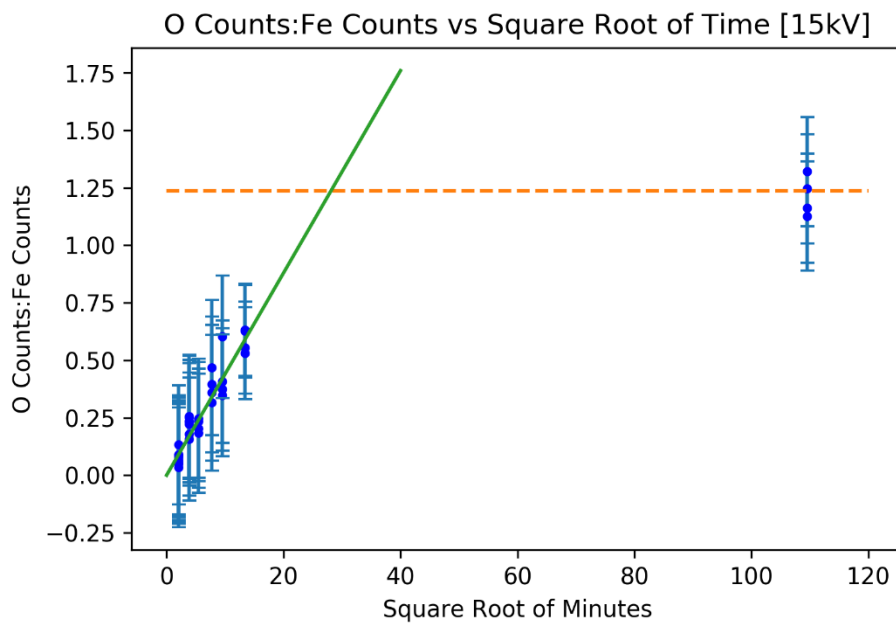


Figure 15: Graph of O Counts:Fe Counts vs the Square Root of Minutes using data taken at 15kV

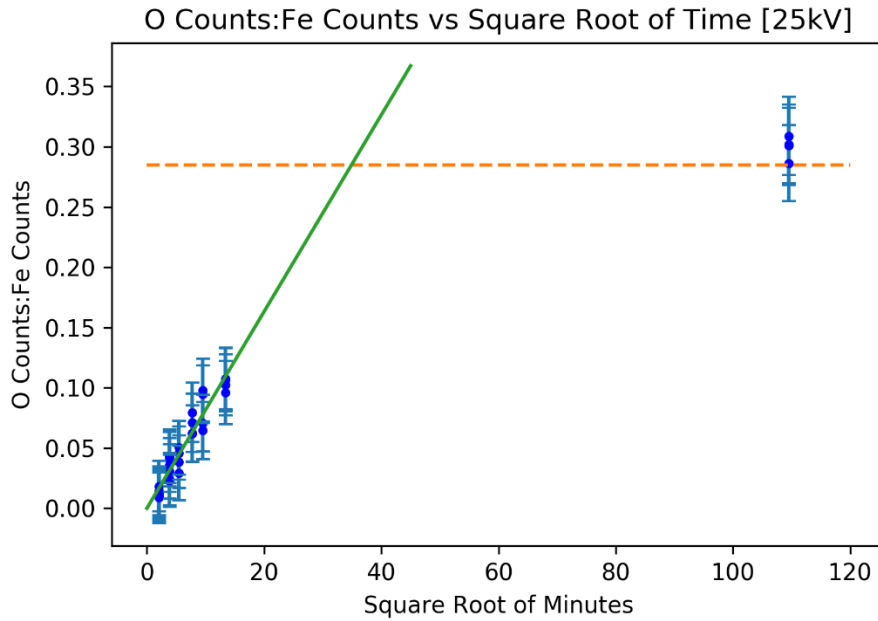


Figure 16: Graph of O Counts:Fe Counts vs the Square Root of Minutes using data taken at 25kV

3.2 Depth Characterization

Translating the oxygen to iron ratio into a concrete characterization of the depth of the corrosion layer is straightforward after a few assumptions.

Figure 14 shows a basic model of a coupon. The shaded region, A, represents the corrosion layer, whereas B represents the steel bulk. As shown by the arrows labeled 15kV and 25kV, an incident electron beam with higher energy will penetrate deeper into the sample. An estimate for the penetration depth in micrometers of an incident beam is given by:

$$x = \frac{0.1E_0^{1.5}}{\rho}$$

Where E_0 is the accelerating voltage in kV and ρ is the density of the sample material in g/cm^3 [3]. To characterize the depth of the corrosion layer, we can begin with the relationship:

$$\left[\frac{O_{measured}}{Fe_{measured}} \right] = \frac{\min(d, x)}{x} \left[\frac{O_{Fe_2O_3}}{Fe_{Fe_2O_3}} \right] + \frac{x - \min(d, x)}{x} \left[\frac{O_{SS304}}{Fe_{SS304}} \right]$$

The measured oxygen to iron ratio is the sum of the oxygen to iron ratios of the corrosion layer and the steel bulk weighted by their relative depths. Here, d is the depth of the corrosion layer and x is still the penetration depth of the electron beam. When choosing whether to use d or x , we simply choose the smaller between the two; this way, the equation saturates when the electron beam cannot penetrate the full depth of the corrosion layer. Assuming a negligible amount of oxygen in SS304, we ignore the second term on the right-hand-side:

$$\left[\frac{O_{measured}}{Fe_{measured}} \right] = \frac{\min(d, x)}{x} \left[\frac{O_{Fe_2O_3}}{Fe_{Fe_2O_3}} \right]$$

Solving for the depth of the corrosion layer:

$$\min(d, x) = \frac{\left[\frac{O_{measured}}{Fe_{measured}} \right] x}{\left[\frac{O_{Fe_2O_3}}{Fe_{Fe_2O_3}} \right]}$$

This is the baseline of our method, and using this expression for the depth of the corrosion layer, we can produce our first depth profile.

Figure 17 shows the corrosion depths produced by the above equation with error bars of one standard deviation.

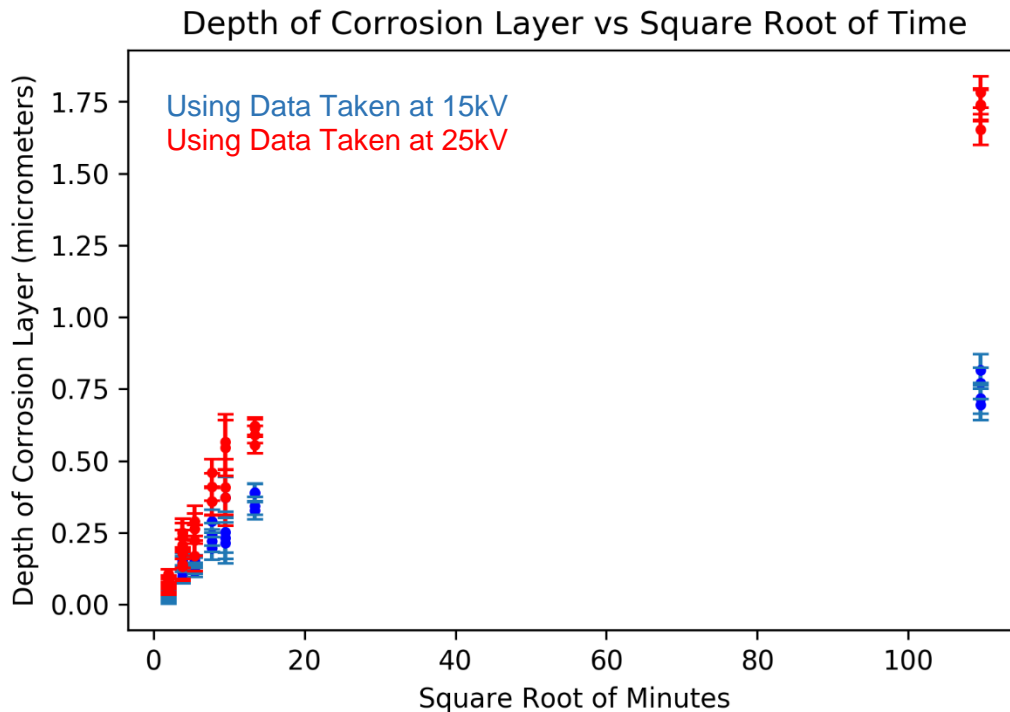


Figure 17: Graph of Depth of the Corrosion Layer vs the Square Root of Time with no corrections

Figure 17 shows that, even without corrections, we can still observe trends in the depth. Immediately we notice a discrepancy between the 15kV and 25kV accelerating voltage data which increases over time. This disconnect is the result of an early assumption: that the density of the material which determines the penetration depth of the electrons is simply that of stainless steel. We know, though, that this is not the case; in fact, the electrons first penetrate the corrosion layer, then pass into the steel bulk. In order to correct for this, we must know both the density of the corrosion layer and the depth of the layer relative to the penetrated depth of the bulk. As mentioned in Section 3.1, it is reasonable to assume that the corrosion layer is comprised at least mainly of Hematite, and the density of Hematite is known to be 5.24 g/cm^3 . As for determining the depth of the corrosion layer, we have already done this in Figure 17.

With reasonable guesses for the density and depth of the corrosion layer, we are ready to make some corrections, namely a new density:

$$\rho' = \frac{d_0}{x_0} \rho_{Fe_2O_3} + \frac{x_0 - d_0}{x_0} \rho_{SS304}$$

Here, d_0 and x_0 are estimated values of the depth of the corrosion layer and the electron penetration depth determined using aforementioned expressions which allow us to introduce ρ' , a corrected density using a weighted combination of the known densities of Hematite and SS304. Using this corrected density in our expression for the electron penetration depth yields:

$$x' = \frac{0.1E_0^{1.5}}{\rho'}$$

And plugging this into our characterization of the corrosion layer:

$$\min(d', x') = \frac{\left[\frac{O_{measured}}{Fe_{measured}} \right] x'}{\left[\frac{O_{Fe_2O_3}}{Fe_{Fe_2O_3}} \right]}$$

By iterating once over this correction, we get a convergence which produces a more agreeable characterization of the depth of the oxide layer shown in Figure 18.

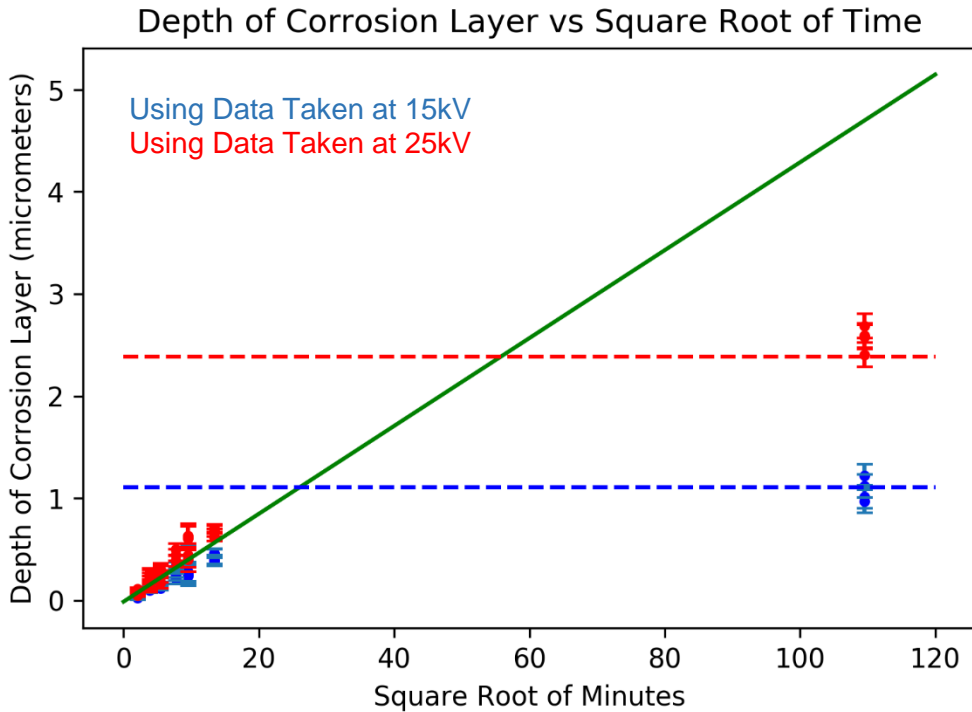


Figure 18: Graph of the Depth of Corrosion Layer vs the Square Root of Minutes with penetration depth saturation levels marked with dotted lines

The corrected values for the depth of the corrosion layer show a characteristically lower discrepancy between the data taken at 15kV and 25kV. It may seem alarming that the predictive trend line rides well above the 200 hour exposure; however, that is once again the artifact of what we call the depth saturation. Because the 15kV and 25kV beams cannot penetrate the full depth of the corrosion layer formed by such a long exposure, the reported depths are merely the penetration depths of the 15kV and 25kV beams.

By examining only the exposure times which produce a corrosion layer depth shallower than the electron penetration depth at accelerating voltages of 15kV and 25kV, we get a better idea of the closeness of the fit; though some points still lie outside

the expected value range. Figure 19 shows the same information as Figure 18, omitting the 200 hour exposure data.

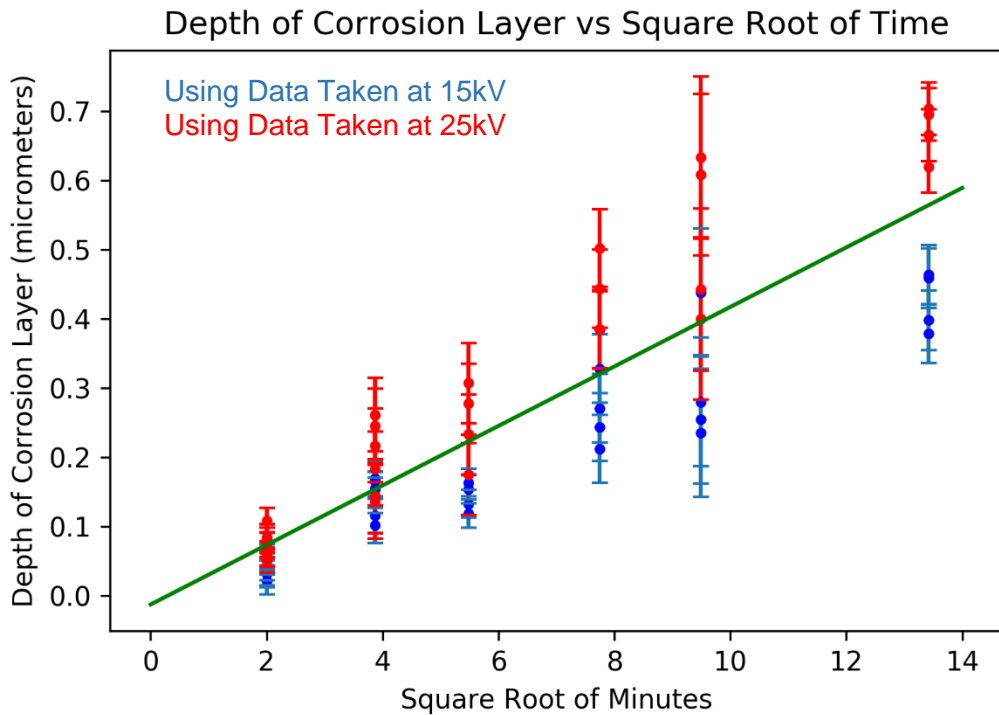


Figure 19: Graph of the Depth of Corrosion Layer vs the Square Root of Minutes showing exposure times up to 3 hours

Error was first estimated using the shift analysis in 2.2.1. From our investigation on the misaligned peaks, we discovered that an offset of one bin (.01 keV) in the energy resulted in a decrease in the oxygen content of about 5%; however, this sensitivity decreased as the oxygen content increased. The contribution of the shift dependence to the error fell orders of magnitude below the standard deviation (σ) of the measurements and was thus not considered in the error calculations used in our plots, which use σ between the four measurements only.

In an attempt to verify and bulk up our data set, we exposed several samples for times between 90 minutes and 12 hours. Given the relative consistency of our previous

results, we were surprised by the data set produced by this most recent exposure pictured in Figures 20 and 21.

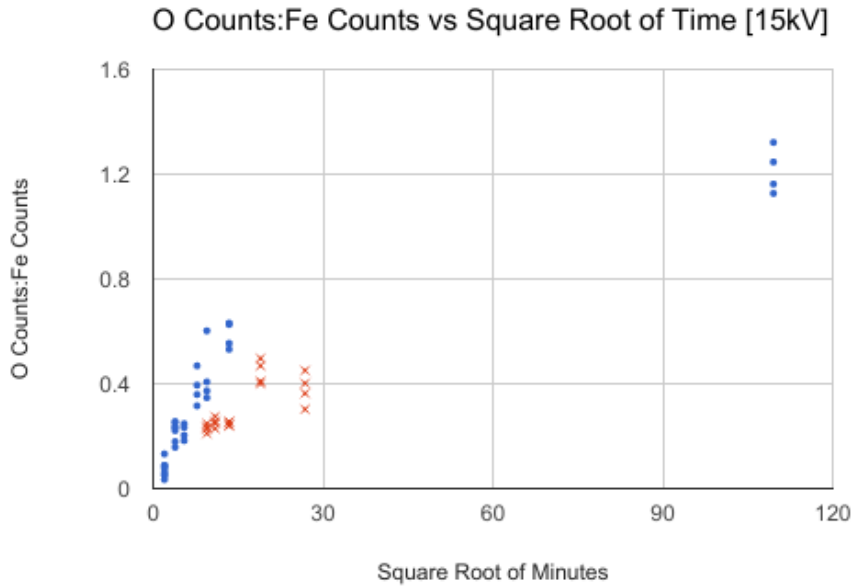


Figure 20: Graph of O Counts:Fe Counts vs the Square Root of Time taken at 15kV showing the old exposure set (blue circles) and the recent exposure set (red x's).

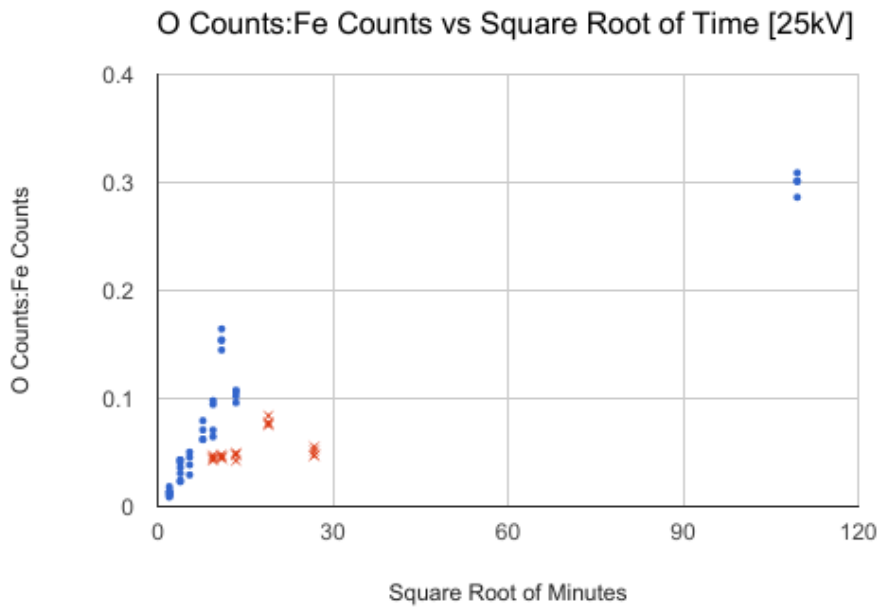


Figure 21: Graph of O Counts:Fe Counts vs the Square Root of Time taken at 25kV from recent set of exposures

We do not understand the behavior of the most recent data set indicated by red x's. Some of the samples seemed to corrode more quickly, while others corroded more slowly. The only known differences in the processing of these samples are that they were electropolished by different people with different amounts of time between the polishing and the exposure. We hypothesize that the variation in corrosion rate is related to one of these two factors. An alternative explanation is that the purity of the salt varied between exposures; we will elaborate on this idea in section 3.3.

3.3 Comparing with Bradshaw and Goods

In their paper, "Corrosion Resistance of Stainless Steels During Thermal Cycling in Alkali Nitrate Molten Salts," Bradshaw and Goods report the descaled weight losses of SS304 samples at 565°C [2]. Their results were plotted as the square root of time with a slope of .031. They described difficulty expressing the formation of the corrosion layer at early times in this manner; as such, most of their work has been at long time scales (hundreds of hours).

As part of our analysis, we compared our depth characterization with the metal loss measurements of Bradshaw and Goods in an attempt to fill in the early portion of their analysis.

Examining only the iron content in Hematite, we get what we will call an iron density of $\rho_{\text{Fe|Hematite}}$ of 3.7 g/cm². Thinking then about the stainless steel bulk of the sample, we determine that, with an atomic percentage of 65% iron, as measured with EDS, the iron density of SS304 is equal to 65% of the density of stainless steel, yielding $\rho_{\text{Fe|SS304}}$ of 4.875 g/cm².

Next, we make the assumption that we lose nickel and chromium in the molten salt as the corrosion layer forms. We verified this by checking ratios of chromium and nickel to iron in both an unexposed sample and a sample that had been exposed to the molten salt for 200 hours. The ratio decreased from 4.88 to .35, verifying a significant loss of chromium and nickel relative to the amount of iron. In making this assumption, we are able to set up the following equality:

$$dA\rho_{Fe|Hematite} = TA\rho_{Fe|SS304}$$

Where d is still the depth of the corrosion layer, A is the surface area of the sample, $\rho_{Fe|Hematite}$ and $\rho_{Fe|SS304}$ are the iron densities aforementioned, and T is the amount of Stainless Steel lost in the corrosion process. Solving for T :

$$T = \frac{d\rho_{Fe|Hematite}}{\rho_{Fe|SS304}}$$

We now have a means to compare to the results of Bradshaw and Goods, who reported their findings in terms of metal lost. We show this comparison in Figures 23 and 24, which show our data alongside that of Bradshaw and Goods, setting their trend lines to intersect the time axis at 0 for comparison purposes. Figure 23 shows the entirety of Bradshaw's and Goods's data set, while figure 24 shows the early regime expanded.

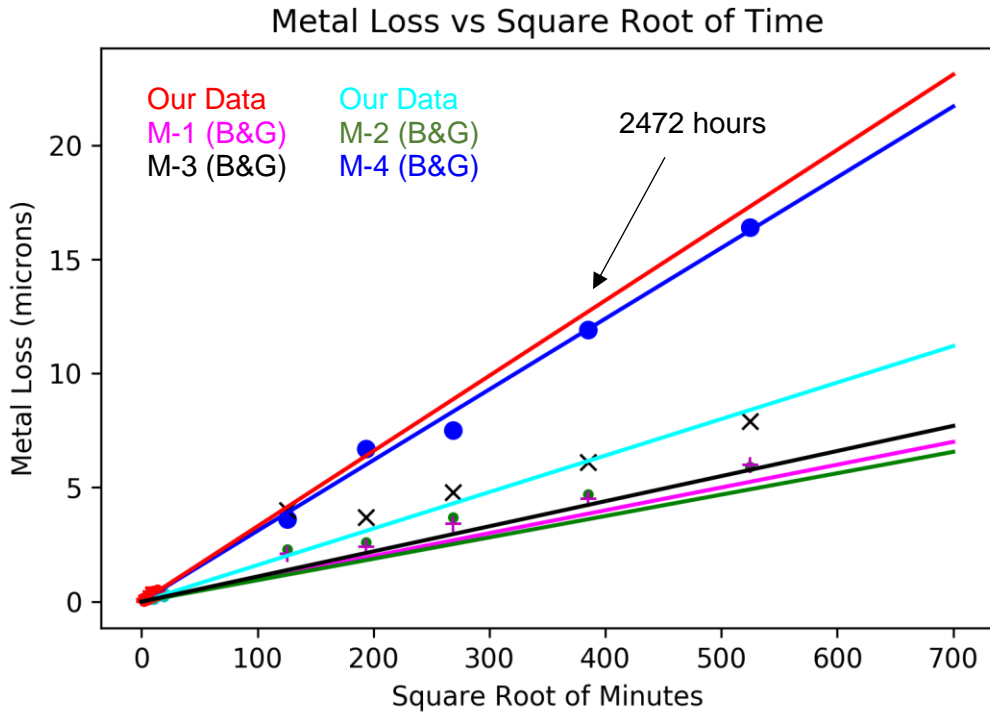


Figure 22: Graph of Metal Loss as a function of the Square Root of Minutes including our data (red and cyan) as well as Bradshaw's and Goods's Data

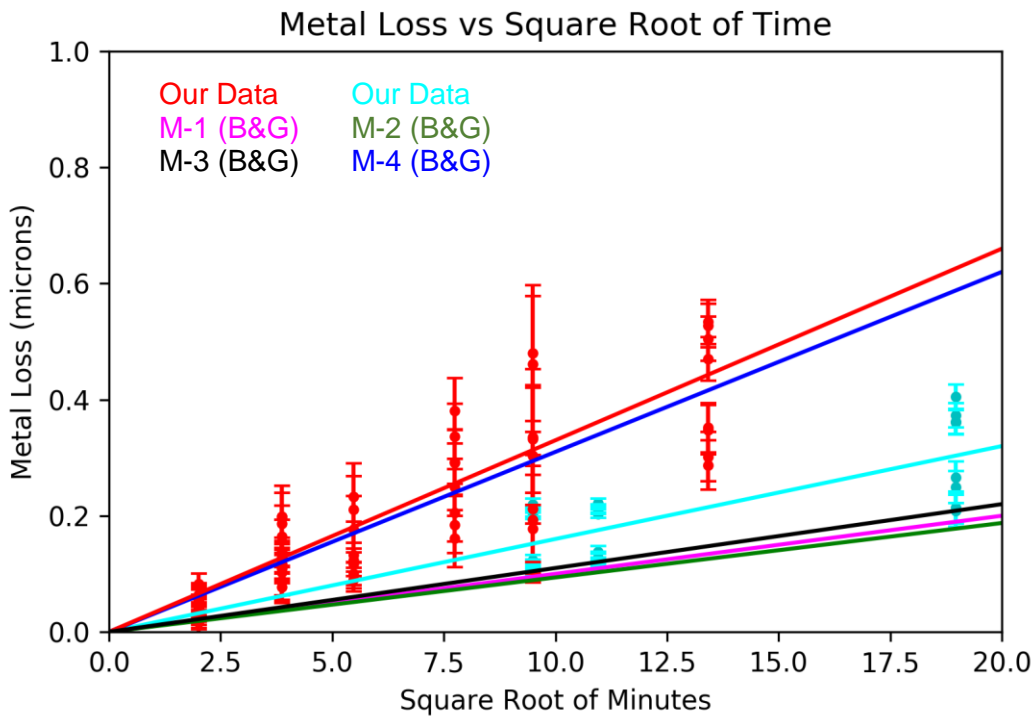


Figure 23: Graph of Metal Loss as a function of the Square Root of Minutes including our data (red and cyan) as well as Bradshaw's and Goods's Data zoomed in to highlight early times

Running our depth characterization through this equation and plotting alongside the results of Bradshaw and Goods, we attempt to show in Figure 23 that even the early growth of the corrosion layer, which they observed as unpredictable and inconsistent, is predictive of the same long-time exposure trends that they observed.

Bradshaw and Goods tested various purities of molten salt, as shown in Figures 22 and 23. The weight percentage of chloride ion impurities in each of the salts is given in parenthesis as follows: M-1 (0.05 Cl⁻), M-2 (0.07 Cl⁻), M-3 (0.55 Cl⁻), M-4 (0.82 Cl⁻). The trend line plotted in red has almost exactly the same slope as that of the M-4 line produced by Bradshaw and Goods. Though it was our understanding that all of our exposures were done with pure solar salt, it is possible that, because the process was not closely supervised by a member of the project for the first set of exposures, the salt may not have been carefully handled prior to the exposure resulting in impurities which contributed to a faster corrosion rate. Using three points from our most recent exposure, the predictive trend line plotted in cyan in Figures 22 and 23 was produced, and it seems to align with the purer solar salts. As this exposure was conducted directly by members of the project, and we are confident that no impurities were allowed to contaminate the nitrate mix, this matches our expectations.

All of that being said, our understanding of exactly what affects the corrosion rate at early times is underdeveloped, and while we were able to produce results which confirmed those of Bradshaw and Goods over long time-scales, we have not been able to reproduce identical data sets of short term exposures; we will discuss this further in Section 4.

4 Discussion

Further verification of this technique could be accomplished in several ways, namely roughness testing and an optical approach.

Using the laser marker, one could conceivably dig a ditch as deep as the oxide layer, then use roughness testing approaches to determine the depth of the engraving. This result could then be compared to the result given by the oxygen to iron ratio method. Though this is a destructive, intrusive technique, it is straightforward and trustworthy. An example of a typical laser hole is pictured in Figure 24.

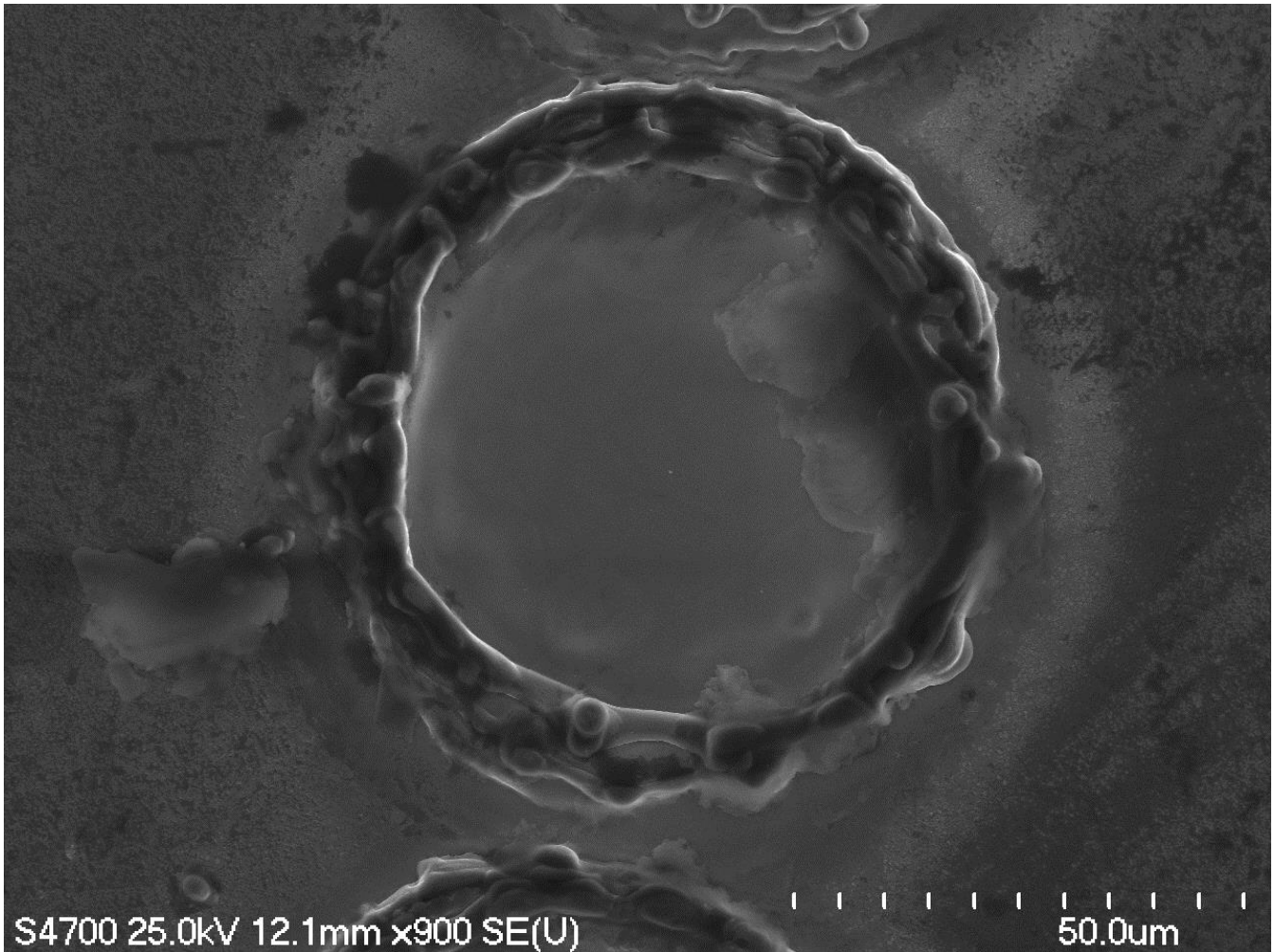


Figure 22: Laser Hole in the corrosion layer of a sample of SS304 exposed to molten salt

An optical approach would involve a similar beginning to the roughness testing, where a hole would be made in the oxide layer, revealing the surface of the stainless steel. Next, a microscope could focus first on the crater, then on the oxide layer, recording the difference between these measurements as the depth of the oxide layer.

We have prepared several samples with electropolishing method outlined in Section 2.1.3 for further testing to better understand the effect of time between polishing and exposure on the growth rate of the corrosion layer and hope to develop and analyze more data sets in the coming months.

5 Conclusion

Our attempt at characterizing the depth of the corrosion layer formed on stainless steel in a molten salt environment with non-destructive techniques was successful. Measurements taken at 15kV and 25kV show a slight discrepancy but overall yield similar results which could likely be brought into closer agreement with further order corrections. Furthermore, predicted results for the depth of the corrosion layer fall in line with what we would expect to measure by penetrating the entire corrosion layer and none of the steel bulk (saturating around 12 hours). Thirdly, our results fall within the same slope range as those of Bradshaw and Goods, predicting accurately the behavior on the order of 1000 hours from data taken from exposures only up to 3 hours [2]. This technique gives a reliable way to characterize the depth of a corrosion layer in a nondestructive manner using EDS techniques.

Acknowledgments

I would like to thank Dr. Cooke for his guidance through this project, as well as Dr. Dennis Manos for his ongoing role in the work. Furthermore, I would like to acknowledge Donley Cormode for her instrumental work on the experiment during the summer of 2016 and Benjamin Kinkaid for training me to use the Phenom to conduct early EDS analysis.

This work was funded by the Office of Naval Research awards N00014-15-1-2770 / UNLV subcontract 71416021B.

References

- [1] 304/304L Data Sheet. West Chester: AK Steel Corporation, 2007. PDF.

- [2] Bradshaw, Robert W. "Corrosion Resistance of Stainless Steels During Thermal Cycling in Alkali Nitrate Molten Salts." (2001): n. pag. Web.

- [3] "Electron Microanalysis Core Facility." *Signals – Electron Microanalysis Core Facility – Northern Arizona University*. N.p., n.d. Web. 12 Apr. 2017.

- [4] EP-Systems. Electro Polish Systems Inc., 2012. Web. 14 Apr. 2016.
<<http://www.ep-systems.com/index.html>>.

- [5] Goods, S. H., and R. W. Bradshaw. "Corrosion of Stainless Steels and Carbon Steel by Molten Mixtures of Commercial Nitrate Salts." (2003). Web. 14 Apr. 2016.

- [6] Li, Xiagang. "Share Corrosion Data." (2015). Web. 14 Apr. 2016.
<<http://www.nature.com/news/materials-science-share-corrosion-data-1.18845>>

- [7] "Molten Salt." *ESolar*. ESolar, Inc, 2016. Web. 12 Apr. 2017.
<<http://www.esolar.com/applications/ms-power/>>.

[8] Thompson, C. V. "Structure Evolution During Processing of Polycrystalline Films." (2000). Web. 14 Apr. 2016.

< <http://www.annualreviews.org/doi/abs/10.1146/annurev.matsci.30.1.159> >